Mon. Not. R. Astron. Soc. **000**, 000–000 (0000) Printed 6 September 2016 (MN LATEX style file v2.2)

Contributions to the accreted stellar halo: an atlas of stellar deposition

N. C. Amorisco[1,2,3⋆]
[1] *Max Planck Institute for Astrophysics, Karl-Schwarzschild-Strasse 1, 85748 Garching, Germany*
[2] *Institute for Theory and Computation, Harvard University, 60 Garden Street, Cambridge, MA 02138, USA*
[3] *Dark Cosmology Centre, Niels Bohr Institute, University of Copenhagen, Juliane Maries Vej 30, DK-2100, Copenhagen*

arXiv:1511.08806v2 [astro-ph.GA] 2 Sep 2016

6 September 2016

ABSTRACT

The accreted component of stellar halos is composed of the contributions of several satellites, falling onto their host with their different masses, at different times, on different orbits. This work uses a suite of idealised, collisionless N-body simulations of minor mergers and a particle tagging technique to understand how these different ingredients shape each contribution to the accreted halo, in both density and kinematics. I find that more massive satellites deposit their stars deeper into the gravitational potential of the host, with a clear segregation enforced by dynamical friction. Earlier accretion events contribute more to the inner regions of the halo; more concentrated subhaloes sink deeper through increased dynamical friction. The orbital circularity of the progenitor at infall is only important for low-mass satellites: dynamical friction efficiently radialises the most massive minor mergers erasing the imprint of the infall orbit for satellite-to-host virial mass ratios $\gtrsim 1/20$. The kinematics of the stars contributed by each satellite is also ordered with satellite mass: low-mass satellites contribute fast-moving populations, in both ordered rotation and radial velocity dispersion. In turn, contributions by massive satellites have lower velocity dispersion and lose their angular momentum to dynamical friction, resulting in a strong radial anisotropy.

Key words: galaxies: kinematics and dynamics — galaxies: structure — galaxies: evolution — galaxies: interaction — Galaxy: halo

1 INTRODUCTION

The abundance of substructure that encircles the Milky Way (e.g. Ibata et al. 1995; Belokurov et al. 2006; Grillmair 2009), Andromeda (e.g. Ibata et al. 2007; McConnachie et al. 2009; Veljanoski et al. 2014), and nearby galaxies (e.g. Martínez-Delgado et al. 2008, 2010; Atkinson et al. 2013; Duc et al. 2015; Crnojević et al. 2016) testifies that at least part of the tenuous stellar haloes that surround galaxies have been contributed hierarchically by smaller merging systems (e.g., Eggen et al. 1962; Searle & Zinn 1978; White & Frenk 1991; Johnston et al. 2008). As a consequence, the detailed properties of individual stellar haloes are the result of a highly stochastic process. This is especially true for Milky Way like galaxies and for galaxies with lower virial mass, where the total budget of the accreted stellar halo is predicted to be dominated by just a handful of satellites (e.g. Bullock & Johnston 2005; Abadi et al. 2006; Sales et al. 2007). For example, evidence is building up that the stellar halo of the Milky Way is quite different from the one of Andromeda, with the first featuring a clearly broken power-law density profile (Deason et al. 2011, 2014, although see also the recent Cohen et al. 2015), while the second displaying an apparently smooth and comparatively shallow density profile out to almost the virial radius (e.g., Gilbert et al. 2012; Ibata et al. 2014).

The origin of this stochasticity lies in the fact that, even after full tidal disruption and complete mixing in phase space, both density and kinematic profiles of the accreted halo keep bearing the signature of the details of the assembly history of the host (e.g., Bullock & Johnston 2005; Cooper et al. 2010; Deason et al. 2013; Pillepich et al. 2014). Just to mention the most important, these details include the masses of the main contributors and their internal structures, their infall times and infall orbits. All these ingredients play a role in determining where and how stars are deposited onto the host, in both density and kinematics, contributing to the stochasticity of the outer stellar halo in potentially different ways. However, a clear theoretical understanding of

⋆ E-mail: nicola.amorisco@cfa.harvard.edu

© 0000 RAS

the role and relevance of these different physical ingredients is still largely missing.

Some correlations have emerged from both observational and theoretical studies. Using stacks of SDSS data, D'Souza et al. (2014) observes that the density slope of the outer stellar envelope is correlated with the stellar mass of the galaxy, but also that galaxies of different morphological types follow different average behaviours. Deason et al. (2013) uses the suite of simulations produced by Bullock & Johnston (2005) to study what kind of accretion histories result in broken density profiles. Though on a rather small sample, they find hints that breaks are more evident in case of quiet recent accretion histories. Finally, Pillepich et al. (2014) perform a thorough study of the outer haloes in the Illustris simulations (Vogelsberger et al. 2014), and find that average density slopes show a significant correlation with both the total virial mass of the host and its formation time: less massive hosts that assemble earlier on display steeper stellar haloes.

Without aiming to produce realistic or detailed models of the stellar halo, I concentrate here on systematically exploring the role of satellite mass, internal structure, infall redshift and infall orbit on shaping the individual contributions to the accreted stellar halo. The objective of the present paper is to investigate where, in terms of orbital energy within the host, different satellites deposit the bulk of their stars. Counterbalancing mechanisms at work are tidal stripping and dynamical friction. Satellites infall on energetically similar, loosely bound orbits (e.g., Benson 2005; Wetzel 2011; Jiang et al. 2015), and then have their energy and angular momentum consumed by dynamical friction, sinking gradually towards the center of the host. At each time, the drag force is instantaneously stronger for more massive remnants, although it can operate for longer times on the less massive subhaloes, which are more resilient to stripping because of their higher concentration. This makes the question of where each satellite releases and deposits its stars while sinking towards the depths of the host potential a non trivial one.

Both tidal stripping and dynamical friction have been widely studied in the literature, as they're vital to a wide range of astrophysical problems. The post-infall evolution of satellite galaxies has been the subject of a number of recent works, both with reference to their subsequent morphological transformation (e.g., Mayer et al. 2001; Kazantzidis et al. 2011; Tomozeiu et al. 2016) to the tidal stripping of their stellar/dark constituents (e.g., Kravtsov et al. 2004; Peñarrubia et al. 2008; Chang et al. 2013; Errani et al. 2015), and to the surviving subhalo populations of hosts within a fully cosmological framework (e.g., Gao et al. 2004; Diemand et al. 2004; Kuhlen et al. 2007; Springel et al. 2008; Ludlow et al. 2009). Recently, van den Bosch et al. (2015) have provided a comprehensive analysis of the significance and extent of segregation in the properties of surviving subhalos, both in terms of their spatial distribution and of their orbital energy. Halo substructure is strongly segregated as a function of the accretion redshift, as the more recently accreted haloes have not yet had the time to sink in. As a direct consequence, subhaloes that are closer to centre of the host (or are on more bound orbits) have lost a higher percentage of their initial mass (e.g. van den Bosch et al. 2015, and references therein).

Table 1. Structural and orbital parameters of the suite of minor merger N-body simulations.

	$M_{\rm vir,s}/M_{\rm vir,h}$	$\log \frac{r_{0,\rm s}/r_{0,\rm h}}{(r_{0,\rm s}/r_{0,\rm h})_{\Lambda\rm CDM}}$	$r_{\rm circ}/r_{0,\rm h}$	j
A	1/122	0	5	{0.2,0.5,0.8}
B	1/50.0	0	5	{0.2,0.5,0.8}
C	1/20.4	0	5	{0.2,0.5,0.8}
D	1/13.0	0	5	{0.2,0.5,0.8}
E	1/8.33	0	5	{0.2,0.5,0.8}
F	1/3.40	0	5	{0.2,0.5,0.8}
G	1/50.0	$0 \pm \sigma\times\{1,2.5\}$	5	0.5
H	1/8.33	$0 \pm \sigma\times\{1,2.5\}$	5	0.5
I	1/50.0	0	9	0.5
J	1/8.33	0	9	0.5

By definition, the works just mentioned concentrate on the properties of the bound remnants, while, motivated by studying the connection with the properties of stellar haloes, here I focus on the tidally shed material, and on whether their kinematics within the host is clearly correlated with the properties of that specific accretion event. In order to address this, I use idealised N-body simulations of minor merger events. A suite of purely collisionless runs is constructed so as to cover those regions of the parameter space that are representative of accretion events in a ΛCDM universe, and that collect the major contributions to the accreted stellar halo.

From the point of view of the methodology, Boylan-Kolchin et al. (2008) have also performed a suite of idealised simulations of minor mergers with different mass ratios and orbital properties. However, their attention was focussed on measuring the time scale of these mergers, and on its dependence on the initial mass ratio and orbital properties.

The structure of this manuscript is as follows: Section 2 presents the numerical setup and illustrates the suite of runs; Section 3 collects the results of this study in dimensionless units; Section 4 scales them to a Milky Way like galaxy, and contextualises findings; Section 5 concentrates on the kinematics of the deposited stars; Section 6 provides a summary of the main findings and lays out the conclusions.

2 SIMULATIONS

As a working hypothesis, I assume that the total density distributions of both hosts and satellites are well described by spherically symmetric, non-rotating NFW density profiles (Navarro et al. 1997). Initial conditions for all simulations are generated from the phase space distribution function of an isotropic NFW structure, exponentially truncated at the virial radius, calculated using Eddington's inversion (Eddington 1916), as delineated by Widrow (2000). As shown by Kazantzidis et al. (2004), this procedure ensures long-term equilibrium, which the assumption of a locally Maxwellian distribution cannot guarantee. All runs are collisionless N-body only simulations, executed using the publicly available code Gadget-2 (Springel 2005). In all cases the satellite is populated with $N_{\rm s} = 5\times10^4$ particles, and all particles in the simulation have similar masses, so that the host is sampled with $N_{\rm h} \approx N_{\rm s}\ M_{\rm vir,h}/M_{\rm vir,s}$ particles. In the following, I will

use the suffixes s and h to indicate, respectively, quantities referring to the satellite and host.

2.1 Stars and dark matter: particle tagging technique

The simulations used here do not explicitly include stellar particles as a separate dynamical component of the merging satellite. Rather, I adopt a particle tagging technique, in which stars are represented by a fraction of the satellite's dark matter particles. These are selected based on their binding energy within the satellite itself. Such particle-tagging strategy has proven to be a successful technique to study the properties of stellar haloes using dark-matter only cosmological simulations (e.g., Bullock et al. 2001; Bullock & Johnston 2005; Cooper et al. 2010, 2013). In particular, Cooper et al. (2010) have shown that a viable tagging criterion should mainly select particles that are deeply embedded within the satellite's halo, as stars form close to the bottom of the gravitational potential. They show that the mass-size relation of galaxies is reasonably fit when stars are identified with the most bound halo particles, up to a threshold $f_{\rm mb}$ of a few percent. Throughout this paper I adopt the nominal value of $f_{\rm mb} = 5\%$. Appendix A explores the effect of reducing such threshold.

A particle-tagging strategy neglects all possible effects that baryonic physics could have on the dark haloes and on the stripping process. Here, for example, it is equivalent to assuming that minor mergers are dominated by a purely collisionless dynamics. The following Section builds on this assumption. I will discuss the limits of the tacit hypotheses that lie behind the particle tagging technique in some more detail in Sect. 6.1.

2.2 The parameter space

In the approximation in which gravitation is the only force at play, in which the gravitational potential of both satellite and host is dark matter dominated, minor mergers can be described within a four-dimensional parameter space. Two dimensionless parameters determine the coupling between the structural properties of satellite and host, and two parameters set the orbital properties of the pair.

A convenient choice for the two structural parameters is the combination

$$\theta_{\rm str} = \left(\frac{M_{\rm vir,s}}{M_{\rm vir,h}}, \frac{r_{0,\rm s}}{r_{0,\rm h}} \right) , \qquad (1)$$

featuring the virial mass ratio between satellite and host, and the ratio between their characteristic radii (equivalently, the latter structural parameter can be replaced by the ratio between the characteristic densities of the two haloes, $\rho_{0,\rm s}/\rho_{0,\rm h}$). Cosmological simulations have shown that the structural properties of ΛCDM haloes are highly correlated, so that halo mass, concentration and redshift are closely related (e.g., Gao et al. 2008; Muñoz-Cuartas et al. 2011; Ludlow et al. 2014, and references therein). This implies that minor merger events that are relevant to a ΛCDM cosmology do not populate the entire plane defined by the parameters (1), but only a well defined region of it. In particular, as the mass-concentration relation at a fixed redshift is essentially scale-free (i.e. a power-law), the locus that identifies

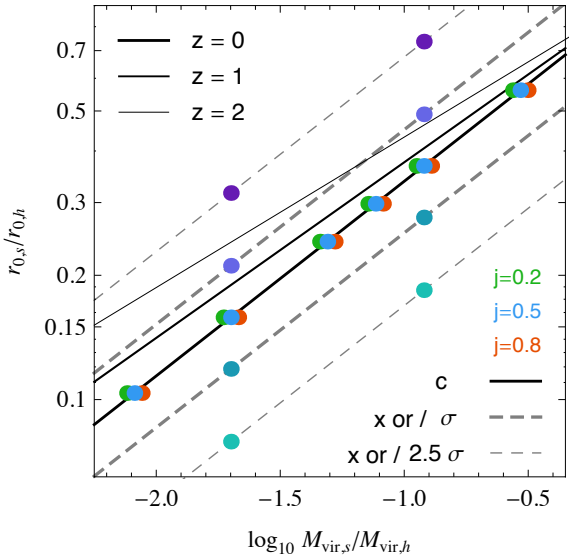

Figure 1. The parameter space describing the structural properties of minor mergers between two NFW haloes: mass ratio and ratio between the scale radii of the two halos, $r_{0,\rm s}/r_{0,\rm h}$. Full lines identify the median scaling relation between these two structural parameters in a ΛCDM universe at different redshifts, as given by the mass-concentration relation. Dashed lines show the effect of the scatter in the mass-concentration relation observed in cosmological simulations. Colored points illustrate how the suite of simulations performed here samples this space (multiple points with different colours indicate runs with different initial orbital circularities).

relevant minor mergers is independent of the host halo mass $M_{\rm vir,h}$.

Full lines in Figure 1 show how the ratio $r_{0,\rm s}/r_{0,\rm h}$ scales with the virial mass ratios $M_{\rm vir,s}/M_{\rm vir,h}$. The Figure concentrates on the range of mass ratios that the most important contributors to the stellar halo are expected to inhabit. Lines of different thickness display the redshift evolution of this locus, for $z \in \{0, 1, 2\}$, i.e. the range of times in which most of the ex-situ stellar mass is expected to be accreted. At higher redshifts the concentrations of haloes of different mass are more similar to each other, implying that the structural ratio $r_{0,\rm s}/r_{0,\rm h}$ is closer to unity than what seen at the present epoch. Dashed lines identify a measure of the characteristic scatter observed in cosmological simulations (e.g., Ludlow et al. 2014), by showing the effect of varying the concentration c of the satellite by a factor of approximately 1 and 2.5 sigma (with respect to its average value at redshift $z = 0$). At constant mass ratio, satellites that are less concentrated than average (or that infall on more concentrated hosts) result in a larger $r_{0,\rm s}/r_{0,\rm h}$, and viceversa.

The two parameters describing the initial orbit of the pair are, respectively, a measure of its energy and angular momentum. Jiang et al. (2015) show that the orbital energy of satellites at infall is comparable with the energy of the circular orbit with radius equal to the virial radius of the host:

$$E_{\rm inf} = E_{\rm circ}(r_{\rm circ}) \quad \text{with} \quad r_{\rm circ} \approx c_{\rm h} r_{0,\rm h} \ , \qquad (2)$$

where $E_{\rm inf}$ is the orbital energy of the satellite at infall, $E_{\rm circ}(r_{\rm circ})$ is the energy of the circular orbit with radius

$r_{\rm circ}$, and $c_{\rm h}$ is the host's concentration. A convenient measure of the initial orbital angular momentum is of course its circularity

$$j \equiv J/J_{\rm circ}(E) \ , \tag{3}$$

so that I adopt the pair of dimensionless parameters

$$\theta_{\rm orb} = \left(\frac{r_{\rm circ}(E_{\rm inf})}{r_{0,\rm h}}, \ j \right) \ . \tag{4}$$

2.3 The suite of runs

Table 1 and Fig. 1 collect the details of the suite of runs. The main contributors to the stellar halo of Milky Way like galaxies are expected to have a mass ratio of $M_{\rm vir,s}/M_{\rm vir,h} \sim 1/10$ (e.g. Bullock & Johnston 2005), so that I explore the range $1/100 \lesssim M_{\rm vir,s}/M_{\rm vir,h} \lesssim 1/3$.

- The main set of simulations (runs A to F) adopts the structural ratio $r_{0,\rm s}/r_{0,\rm h}$ identified by cosmological simulations for the corresponding mass ratio at redshift $z = 0$ (see Fig. 1).
- A parallel set of runs (G and H) explores the effect of the scatter expected in the structural properties of haloes. Note that such scatter fully includes any shifts due to the systematic change in the structure of haloes at different infall redshifts, at least while $z_{\rm inf} \lesssim 2.5$.
- I consider two values of the initial orbital energy $E_{\rm inf}$: $r_{\rm circ}/r_{0,\rm h} \in \{5, 9\}$. These approximately contain the interval that is representative of accretions onto a Milky Way sized haloes at intermediate redshifts. Runs I and J are used to estimate the effect of this additional degree of freedom.

Finally, cosmological accretions have circularities at infall that are centred on intermediate values, $j \approx 0.5$, but with a significant spread towards both radial and circular orbits (e.g., Jiang et al. 2015). In order to explore the full allowed range, I consider the cases $j \in \{0.2, 0.5, 0.8\}$ (runs A to F). As orbital energy stays fixed, each simulation begins with the satellite at different apocentric distances. In turn, before the effect of dynamical friction, these orbits have very similar orbital times, which are mainly a function of energy.

All simulations are run for a total time that corresponds to 15 Gyr when $M_{\rm vir,h}$ is scaled to $10^{12} M_{\odot}$. It is worth mentioning that not all satellites are entirely destroyed by this time. The most massive satellites I consider here are quickly disrupted within a couple of pericentric passages, but the lowest mass ones survive for much longer and are considerably more resilient to tides as a result of the much higher contrast between their central density and the density of the host. For example, for all circularities, even after 15 Gyr, the satellites in runs A, with the lowest mass ratio, still display a bound nugget of about a few percent of the initial virial mass. This is also true for the highest-circularity and highest-concentration cases of run B. At the resolution used here, all other minor mergers are complete within the time interval covered by the studied runs.

3 MASS DEPOSITION

A visual impression into the unfolding of the minor mergers is displayed in Figure 2, which shows the relative orbital

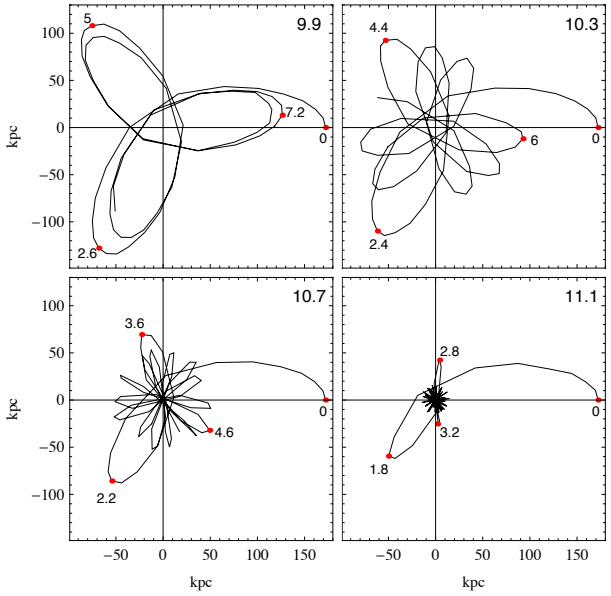

Figure 2. The relative orbit of the satellite's and host's most bound particles. Satellite masses (indicated in the upper-right corner of each panel) have been scaled to the case of a Milky Way like host, $M_{\rm vir,h} = 10^{12} M_{\odot}$. The same physical scaling has been applied to the orbital times, displayed for the sequence of the first four apocenters. All panels refer to the case $j = 0.5$, with $r_{0,\rm s}/r_{0,\rm h} = (r_{0,\rm s}/r_{0,\rm h})_{\Lambda\rm CDM}$, runs A, B, C, E.

distance between the satellite's and host's most bound particles, for the case $j = 0.5$ and $r_{0,\rm s}/r_{0,\rm h} = (r_{0,\rm s}/r_{0,\rm h})_{\Lambda\rm CDM}$ (runs A, B, C and E). To simplify the interpretation, displayed quantities have been scaled to the case of a Milky Way like host at redshift $z = 0$, with $M_{\rm vir,h} = 10^{12} M_{\odot}$ and $r_{0,\rm h} = 21.1$kpc. Each panel reports the logarithm of the satellite masses in the upper-right and the orbital times of the first four apocentric passages in Gyr. The evolution in the apocentric distances shows that, in all cases, dynamical friction drags the satellite towards a more bound orbit. Energy is lost during some initial period of time, during which a massive-enough bound remnant is present, but the length of which depends on the initial satellite mass. Thereafter, energy is conserved until the end of the simulation, with no further orbital evolution.

Fig. 2 is already showing that, all the rest being equal, dynamical friction is more effective on the more massive satellites. Although low-mass subhaloes survive for much longer, their sink rate is too low to allow them to reach the central regions of the host. In fact, they are confined to the outskirts, where they dissolve very slowly under the influence of tides.

3.1 Dynamical friction at play

Figure 3 provides a quantitative view on the effect of dynamical friction. For different mass ratios, panels display scatter plots of the final energy of each satellite particle within the merger product against its initial energy within the satellite itself. More explicitly, $(E/\Phi_{\rm min})_{\rm merg}$ is the orbital energy of particles at the end of the simulation, normalised by the depth of the potential well. For example, the horizontal dashed line present in all panels of Fig. 3 identifies the

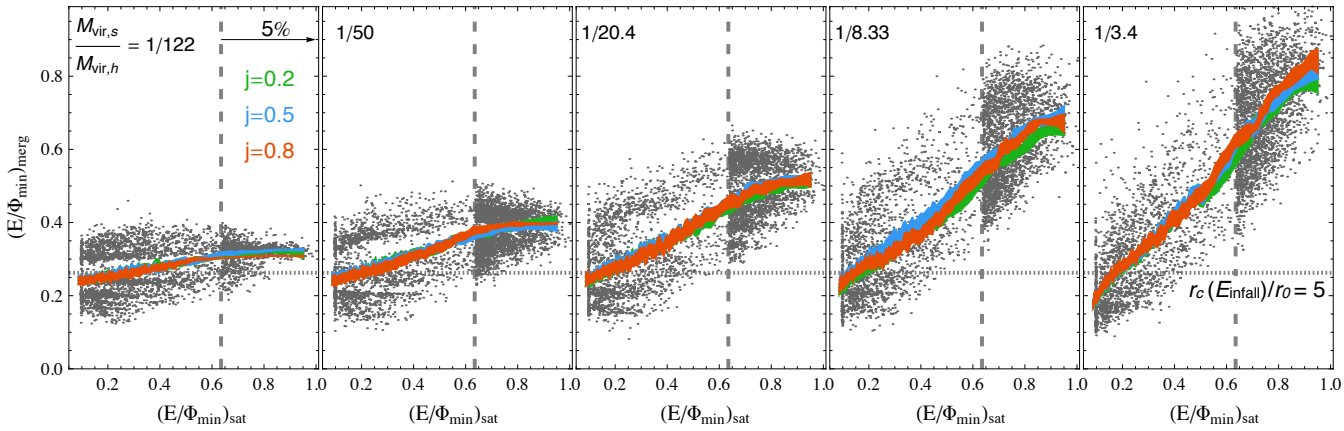

Figure 3. The energy distribution of the satellites particles. The panels show the scatter plots of the final (normalised) energy of the satellite's particles within the host (on the y axis), as a function of their initial (normalised) energy within the infalling satellite before interaction (on the x axis). Higher values in both coordinates represent particles that sit deeper within the final host's or initial satellite's potential. Tidal stripping of the satellite proceeds in time from left to right, removing increasingly more bound particles. Dynamical friction operates dragging the satellite's remnant towards the top of each panel, deeper into the host. Panels illustrate the effect of different initial virial mass ratios, displayed in the top-left of each panel. Different colours in all panels are used to highlight median values (with one-sigma uncertainty) for infall orbits with different initial circularity: $j \in \{0.2, 0.5, 0.8\}$, as in the legend in the leftmost panel. Grey points always refer to the case $j = 0.5$; for convenience, only 10% of the dark matter particles are actually displayed (to the left of the vertical dashed line identifying the stellar particles). Dynamical friction causes more massive satellites to deposit their stars deeper into the host's potential, with a clear gradient.

orbital energy of the satellites at infall. Particles with large values of $(E/\Phi_{\rm min})_{\rm merg}$ are more deeply bound within the merger product, up to $(E/\Phi_{\rm min})_{\rm merg} = 1$, which identifies a particle sitting at rest at the centre of such a potential well. Analogously, $(E/\Phi_{\rm min})_{\rm sat}$ is the normalised energy within the satellite before infall, and therefore measures how bound particles were within it before the merger event. Stars sit at the bottom of the potential wells of the satellites, and are therefore to the right end of all panels. In fact, the vertical dashed lines separate the 5% most bound particles in the satellite itself. As described in Sect. 2.1, these are tagged as stars. Tidal stripping proceeds from left to right in each of the panels of Fig. 3: particles that are less bound to the satellite are lost earlier. With time, dynamical friction gradually drags the satellites remnant closer to the centre of the host, towards the top of each panel, causing particles that were initially more bound to also be tidally stripped.

Grey points in the different panels of Fig. 3 illustrate the cases $j = 0.5$ and $r_{0,\rm s}/r_{0,\rm h} = (r_{0,\rm s}/r_{0,\rm h})_{\Lambda\rm CDM}$ (runs A, B, C, E, F). For each mass ratio, coloured lines display medians (with associated 1-sigma uncertainty) for the three runs with different initial circularities, as indicated in the leftmost panel. At a given binding energy within the satellite $(E/\Phi_{\rm min})_{\rm sat}$, the distribution of energies within the host $(E/\Phi_{\rm min})_{\rm merg}$ is bimodal around the median. Particles with higher (lower) values were lost in the leading (trailing) condition (e.g., Johnston 1998; Amorisco 2015), when the remnant had approximately the corresponding median energy value. The distribution of particles in the scatter plots is also non-homogeneous, featuring for example clear overdensities in the form of horizontal streaks. These represent collections of particles with very similar energies in the host, lost together in a coherent manner, which is what happens at pericentric passages.

For all mass ratios and for all initial circularities, the least bound particles within the satellite are also the least bound particles within the merger product at the end of the run. Their energies are distributed around the initial orbital energy of the satellite at infall. Particles that were more tightly bound within the satellite are correspondingly more bound within the host, with a clear gradient enforced by dynamical friction. The existence of such a gradient is not new in the literature, and in fact an expression of the tendency of collisionless mergers to preserve the rank order of particles in energy (White 1978, 1980; Barnes 1988; Hopkins et al. 2009). What is most interesting here, however, is that the slope of the same gradient is a strong function of the satellite mass. Only the most massive minor mergers are capable of delivering their stars deep into the central regions of the host. In turn, the initial orbital circularity does not represent an important factor in this respect, with the differently coloured medians being practically indistinguishable in all panels.

Figure 4 shows the spherically averaged density profiles of the stars deposited in the final merger product, with associated one-sigma uncertainty. Satellite masses grow from left to right and the colour coding in each panel is the same as in Fig. 3, indicating different initial orbital circularities. All density profiles are scaled so to integrate to the same total mass. First, it is evident that more massive satellites imply higher central densities, which is a direct outcome of the gradient observed in Fig. 3 in energy-space. Vertical coloured lines in Fig. 4 show the half-mass radius $r_{0.5}$ of each stellar density profile. As a consequence of the gradient in the effectiveness of dynamical friction, half mass radii become smaller for higher satellite masses (Appendix A explore the dependence of the half-mass radius with the chosen tagging fraction $f_{\rm mb}$). Second, the initial circularity is only important at low satellite masses, where the density profiles resulting from satellites infalling on more circular orbit dis-

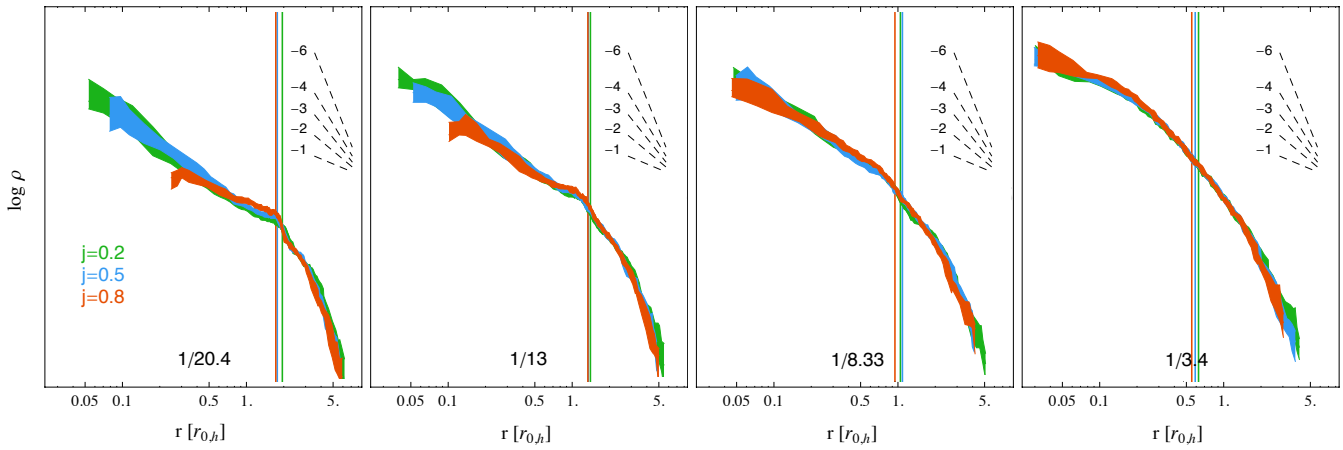

Figure 4. The final density distribution of the deposited stars (the most bound 5% of the satellite particles). Panels illustrate the effect of different virial mass ratios, as indicated in the bottom of each panel. Different colours in all panels are used for infall orbits with different initial circularity: $j \in \{0.2, 0.5, 0.8\}$, as in the legend in the leftmost panel. All profiles are normalised to the same total mass, showing that more massive satellites cause higher central densities, by depositing their most bound particles deeper in the host potential. Vertical coloured lines display the half-mass radius associated to each density profile.

play central density holes. In turn, for massive satellites, the density profiles resulting from accretion events with different circularities at infall are practically indistinguishable. The reason for this is explored in Section 5, which concentrate on the kinematics of the deposited material. Finally, there is a trend in the structure of the density profiles with satellite mass: low mass satellites result in more clearly broken density profiles, with a radius in which their logarithmic slope evolves sharply; massive subhaloes deposit stars in apparently smooth density profiles, with a gentle and progressive steepening of the logarithmic slope.

3.2 The effects of concentration and orbital energy at infall

The results presented so far pertain to the median population of ΛCDM haloes, with runs A to F adopting the prescription $r_{0,\rm s}/r_{0,\rm h} = (r_{0,\rm s}/r_{0,\rm h})_{\Lambda\rm CDM}$. Figure 5 illustrates the effect of the scatter in the concentration of the satellite haloes. As mentioned in Sect. 2, runs G and H adopt shifts to the halo concentration of the satellites corresponding to factors of approximately $\{1, 2.5\} \times \sigma_c$, where σ_c is the (logarithm of the) scatter observed in cosmological simulations (e.g., Ludlow et al. 2014). The colour-coding is the same used in Fig. 1, so that the nominal run, with $r_{0,\rm s}/r_{0,\rm h} = (r_{0,\rm s}/r_{0,\rm h})_{\Lambda\rm CDM}$ is always shown in turquoise, and is accompanied by the full particle scatter plot (grey points).

Satellites that are less concentrated than average (or that infall on hosts that are more concentrated than average) do not manage to reach as deep into the host potential as their analogues with the same initial mass. Of course, this is a result of a quicker tidal stripping: less concentrated satellites are less dense and lose mass at a quicker rate, which does not allow dynamical friction to consume a similar amount of orbital energy. The effect of concentration is quite marked on the resulting density profiles and half-mass radii of the deposited stars. The concentrated satellites contribute stellar populations with much higher central densities, with smoothly falling density profiles, without sharp breaks. In turn, stars contributed by low-concentration satellites feature more marked breaks at large radii and their spatial distribution is considerably more diffuse. As shown in Fig. 1, at fixed mass ratio, earlier accretions are characterised by higher values of the structural ratio $r_{0,\rm s}/r_{0,\rm h}$, i.e. lower values of the density contrast, and are therefore equivalent to mergers with slightly less concentrated satellites. From a purely structural point of view, this results in comparatively less deep contributions to the stellar halo, although this effect remains minor with respect to the physical evolution of the host, as it will be shown in the following Section.

Accretion events happening at higher redshift also differ for their average orbital energy, as $r_{\rm circ}/r_{0,\rm h} \approx c_{\rm h}$ (e.g., Jiang et al. 2015). As the concentration of the host increases monotonically with redshift, accretions at higher redshifts begin at slightly more bound initial normalised orbital energies. In order to investigate any effect of this evolution on the final location of the stellar debris, Fig. 7 compares runs with $r_{\rm circ}/r_{0,\rm h} = 5$ and $r_{\rm circ}/r_{0,\rm h} = 9$ (respectively, runs B E and I J). I find that a more loosely bound initial condition (i.e. $r_{\rm circ}/r_{0,\rm h} = 9$, meaning a more recent accretion event) results in symmetrically more extended contributions to the stellar halo. Note in particular the apparent similarity of two colored median tracks, which are are essentially parallel to each other: a shift in the initial infall orbital energy results in a shift in the final mean energy of the deposited material. Finally, there is perhaps a mild difference in the shape of the stellar density profile resulting from the two cases, with the higher-energy case $r_{\rm circ}/r_{0,\rm h} = 9$ featuring a somewhat better defined density break.

4 REDSHIFT EVOLUTION: ACCRETIONS ONTO A MILKY WAY LIKE GALAXY

In this Section, I use the results described so far, laid out in structural dimensionless units, to derive scalings in physical units representative for accretions onto a Milky Way like galaxy. I have shown that the half-mass radius $r_{0.5}$ is

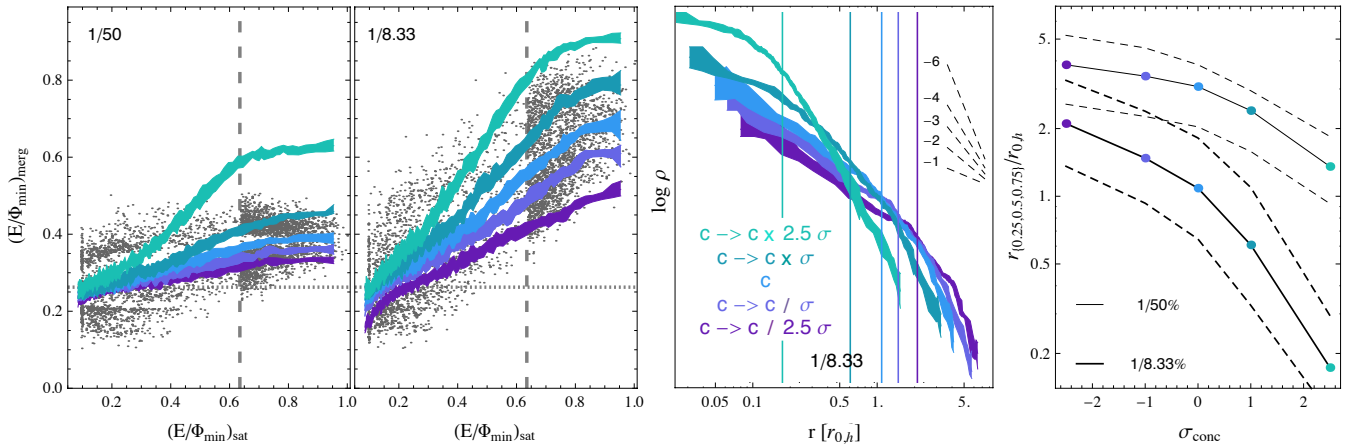

Figure 5. The effect of satellite concentration. Different colours compare the final energy and density distributions of the stars deposited by satellites with different concentrations, probing an interval equivalent to $\approx \pm 2.5\sigma_c$ observed in cosmological simulations. Vertical lines in the third panel display the half-mass radii of each plotted density profile. These are plotted as a function of the shift from the mean concentration in the rightmost panel, together with the radii $r_{0.25}$ and $r_{0.75}$, containing respectively 25% and 75% of the stars, for two values of the satellite-to-host virial mass ratio. Satellites with higher concentrations sink further in before releasing their most bound particles, resulting in more concentrated, smoother accreted stellar profiles. As in Fig. 3, grey points refer to the case with average concentration and initial $j = 0.5$, with an analogous change in sampling across the 5% vertical line.

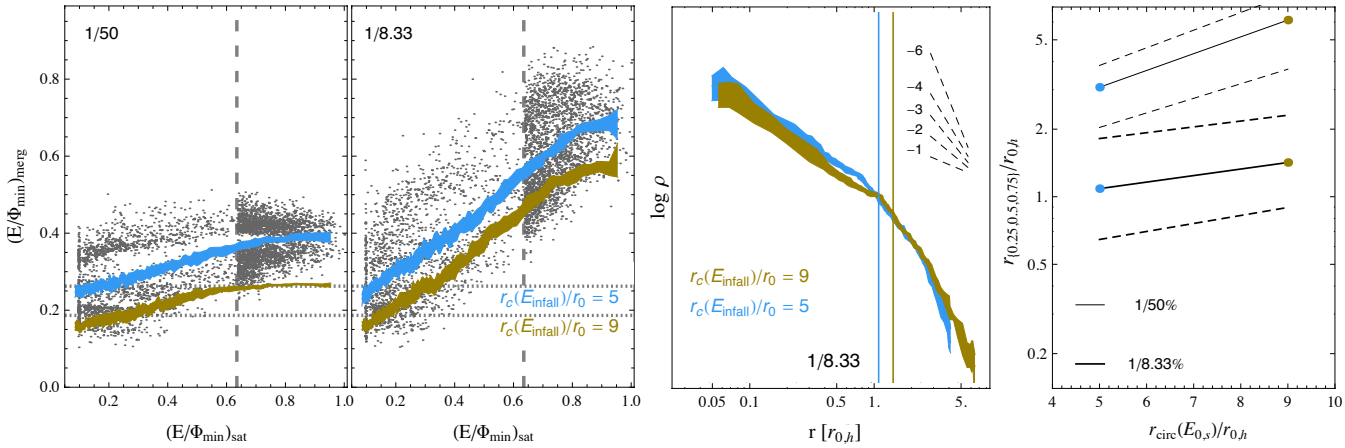

Figure 6. The effect of the initial orbital energy at infall. Different colours compare the density and energy distributions resulting from satellites with different orbital energies, covering approximately the interval expected for recent accretions events on Milky Way like galaxies ($r_{circ}/r_{0,h} = 9$) to accretions at intermediate redshifts $z_{inf} \approx 2$ ($r_{circ}/r_{0,h} = 5$). Vertical lines in the third panel display the half-mass radii of each plotted density profile. These are plotted as a function of infall orbital energy in the rightmost panel, together with the radii $r_{0.25}$ and $r_{0.75}$, containing respectively 25% and 75% of the stars. As in Fig. 3, grey points refer to the case with average concentration and initial $j = 0.5$, with an analogous change in sampling across the 5% vertical line.

practically insensitive to the initial orbital circularity of the satellite, and therefore it represents a useful quantity to explore the effect of the other ingredients at play. In particular, here I concentrate on satellite mass and infall redshift.

As mentioned in Sect. 2, structural parameters of average ΛCDM minor mergers at redshifts $z_{inf} \lesssim 2.5$ lie within the area covered by the scatter in the concentration-mass relation at the present epoch. Therefore, I can derive the structural properties of accretion events at intermediate redshifts by interpolating the results of the runs presented here. As to physical scales, I adopt that, at $z = 0$ a Milky Way like host has $M_{vir,h} = 10^{12} M_\odot$, and that at all times, it was in good agreement with the average properties observed in cosmological simulations. This assumption regards both its mass accretion history (which I assume follows a median accretion history as compiled by Fakhouri et al. 2010), and its concentration (which, for consistency, I assume follows the median relation of the Millennium haloes as compiled by Gao et al. 2008). Therefore, for example, the host halo currently has a characteristic radius of $r_{0,h}(z = 0) \approx 21$kpc, while this was about $r_{0,h}(z = 2) \approx 16.5$ kpc at higher redshift, when its mass was $M_{vir,h} \approx 10^{11.55} M_\odot$. I use the scale radius of the halo r_0 at the time of accretion to scale the dimensionless density profile of the deposited material. This implies I am ignoring the effect that any subsequent evolution of the host (which has been shown to be limited, e.g., Buist & Helmi 2014) may have on the phase space coordinates of the deposited stars.

Before describing results, it is fair to mention that these should be regarded only as educated estimates, due to the

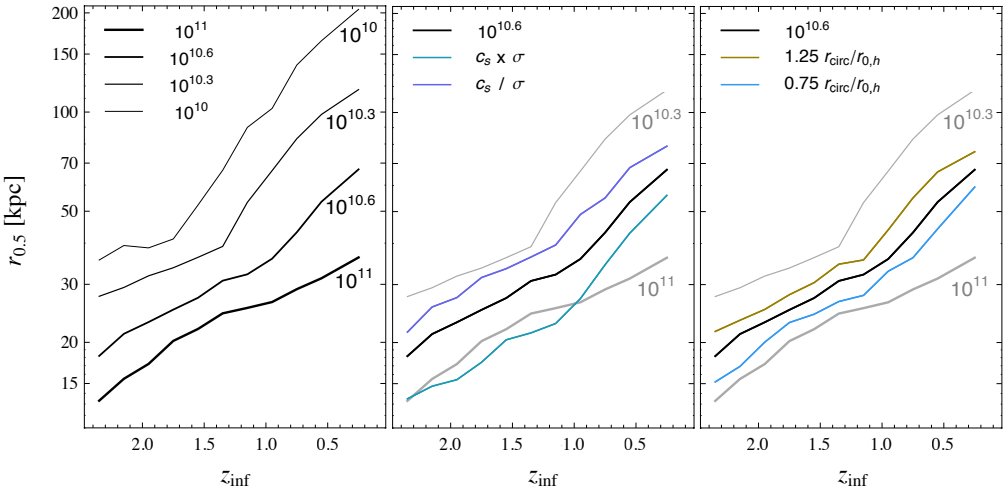

Figure 7. The final half-mass radius $r_{0.5}$ for contributions to the stellar halo of a Milky Way like galaxy, by satellites of different masses (lines of different thickness), infalling at different redshifts $z_{\rm inf}$. Middle and right panels compare the pure influence of mass and redshift to the effects of satellite concentration and orbital energy at infall.

several working hypotheses on which they depend. In order of importance, I am assuming that: (i) the host is 'average' at all times since $z \approx 2.5$; (ii) the influence of any stellar component in the host on the dynamics of the minor merger can be neglected (which may be worrisome because of the dynamical effects of the disk, see for example Peñarrubia et al. 2004; Monachesi et al. 2015a); (iii) satellites are strongly dark matter dominated, and the tagging criterion $f_{\rm mb} = 5\%$ well describes their stellar components; (iv) once stars are deposited by each satellite, the host's mass growth has a negligible effect on their density profiles, which also means that the host has not experienced major mergers since.

Under this set of assumptions, the left panel of Figure 7 shows the evolution of the half-mass radius $r_{0.5}$ with both the virial mass of the satellite (lines of different thickness in the left-most panel) and for different infall redshifts. Note that, while in all previous plots I have used fixed values of the satellite to host virial mass ratio, here I am using the actual satellite's virial mass at infall. Therefore, as a result of the mass evolution of the host, different lines imply a mass ratio that increases slightly with redshift. I have already shown that more massive satellites deposit stars deeper into the host potential, and this is clearly visible in Fig. 7. Additionally, Fig. 7 is showing a clear gradient with infall redshift $z_{\rm inf}$: for equal satellite masses, stars deposited by earlier accretions can now be found closer to the host's centre. This effect has also been seen by Pillepich et al. (2014), that measure that the stellar haloes of galaxies with a quicker assembly history (earlier halo formation time) display steeper density profiles, and are therefore more compact.

The driving effect of this evolution is in the size evolution of the host. The scale radius of the host's halo grows monotonically with redshift, implying that similar dimensionless radii are scaled to larger physical radii in the host for more recent accretions. Additionally, at higher redshift the host's concentration is also lower, implying initially more bound energies at infall, the effect of which has been illustrated in Sect. 3.2. The combination of these two mechanisms is particularly important for the low mass satellites, where the counter-effect of dynamical friction has little influence. Satellites infalling more recently are dragged more strongly by dynamical friction, as a result of their higher density contrast (see Fig. 1). However, this effect is practically negligible for those satellites with $M_{\rm vir,s}/M_{\rm vir,h} \lesssim 1/50$, where dynamical friction is almost negligible. Therefore, the half-mass radius of the stars deposited by the satellites with the lowest mass explored in Fig. 7 evolves by almost an order of magnitude between accretions at redshift $z_{\rm inf} \approx 2.5$ and very recent events. Note, however, that some of such low mass satellites with very recent accretion redshift might not have been entirely stripped of their stars at redshift $z = 0$. This is an effect that is not explicitly considered in Fig. 7.

After satellite mass and infall redshift, the leading factor in shaping stellar deposition is the satellite's concentration, the effect of which is shown by the middle panel of Fig. 7. A shift of a factor one-sigma in the satellite's concentration results in changes to the half mass radius of the deposited stars that is roughly similar to what a factor of ≈ 2.5 in mass would cause. In turn, the average scatter in the orbital energy at infall (Jiang et al. 2015) has a comparatively smaller importance, as shown by the rightmost panel.

5 KINEMATICS OF THE CONTRIBUTED STARS

In this Section, I concentrate on the orbital properties and kinematical profiles of the material contributed by each accretion event. This subject is closely connected to the orbital evolution of the satellite, as particles are lost with energies and angular momenta that are close to the ones of the remnant at the time of their escape (e.g. Johnston 1998; Amorisco 2015). Therefore, whether the orbits of the contributed stars are preferentially radial or circular mainly depends on the properties of the remnant's orbit during its disruption.

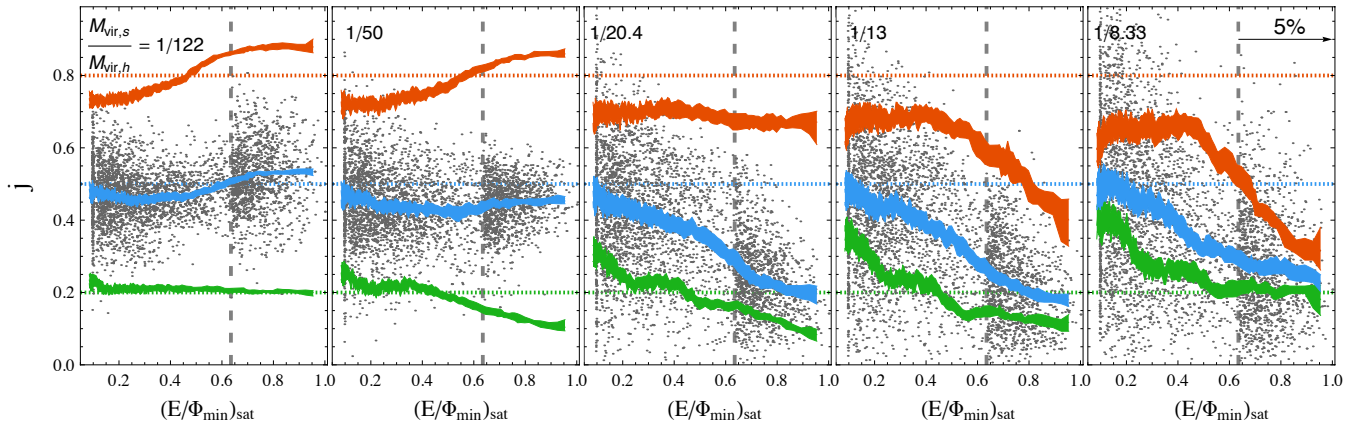

Figure 8. Final circularities of the satellite's particles within the merger remnant. As in Fig. 3, the satellite's particles are ordered according to their binding energy within the satellite itself, prior to the merger. The y axis shows the orbital circularity of each particle within the host after it escapes the satellite, at the end of the simulation. Colour coding is analogous to Fig. 3, horizontal dotted lines show the values of the initial orbital circularity of the satellite at infall. Grey points refer to the case with $j = 0.5$, with the same change in sampling (across the 5% vertical line) adopted in Fig. 3 and 5.

5.1 Orbital evolution and radialisation

Unfortunately, it is not possible to assume that the orbital circularity of the remnant remains constant during the satellite's disruption for all initial mass ratios and circularities at infall. Processing by dynamical friction may cause significant evolution between infall and the time when stars are lost. When used with a constant Coulomb logarithm, the dynamical friction formula derived by Chandrasekhar (1943) suggests orbital circularisation. However, historically, the comparison between the prediction of this simplified formula and results of actual N-body simulations has met with mixed success (e.g. Velazquez & White 1999; Jiang & Binney 2000; Taylor & Babul 2001; Hashimoto et al. 2003). Reasons for this are that: (i) in opposition to Chandrasekhar's framework, the Coulomb logarithm is an evolving quantity in a merger; (ii) material that has just been lost from the satellite can still contribute to the density wake, and therefore increase the rate of energy and angular momentum loss (e.g., Fujii et al. 2006; Fellhauer & Lin 2007).

Figure 8 explores the evolution of the orbital circularity of the remnant through the final circularity of its particles within the merger remnant. The structure of Fig. 8 is analogous to the one of Fig. 3: the x axis is the normalised binding energy of the satellite particles within the satellite itself, the y axis shows the circularity of such particles in the merger remnant, at the end of the simulation. Stars are those particles to the right of the vertical dashed line, which identifies the tagging threshold $f_{mb} = 5\%$. As in Fig. 3, coloured areas illustrate median values (with associated one-sigma uncertainty) for satellites infalling with different initial circularities, as shown by the horizontal dotted lines. As in Fig. 3, tidal stripping, dynamical friction and time all proceed from left to right in each panel. Therefore, median tracks with a positive gradient indicate a circularising progenitor, while a negative gradient identifies an evolution towards a more radial orbit. As for Fig. 3, grey points within each panel illustrate the case $j_{inf} = 0.5$.

There are a few points worth noticing.

- As it could be expected, the satellites particles that are least bound to the satellite itself cluster in general close to the initial orbital circularity of the progenitor at infall. However, with increasing satellite mass, the median circularity at low values of $(E/\Phi_{min})_{sat}$ departs from the nominal initial orbital circularity of the satellite. This is not an effect of dynamical friction, but the result of the growing internal velocity dispersion of the satellite, which 'dilutes' the imprint of the bulk orbital velocity. For example, the median circularity of the least bound particles in massive satellites infalling with $j_{inf} = 0.8$, grows lower than this figure. Symmetrically, it gets higher than $j_{inf} = 0.2$ for those massive satellites infalling on almost radial orbits.
- In proceeding towards particles with higher and higher values of the binding energy $(E/\Phi_{min})_{sat}$, the scatter around the median circularity within the host decreases. This is a consequence of the decreasing bound mass of the remnant, which implies a decreasing scatter in the kinematic properties of the particles at the time of shedding.
- Low mass satellites that infall on quite circular orbits experience some mild circularisation. This happens in both cases $M_{vir,s}/M_{vir,h} \in \{1/122, 1/50\}$ when infalling with $j_{inf} = 0.8$. Satellites of similar masses either do not experience significant evolution in their orbital circularity (like in the case $j_{inf} = 0.5$), or are dragged towards even more radial orbits (like for the case $j_{inf} = 0.2$ and $M_{vir,s}/M_{vir,h} = 1/50$).
- Satellites with higher masses, independently of their infall circularity, are uniformly dragged towards more radial orbits. This is especially evident at intermediate satellite masses, $M_{vir,s}/M_{vir,h} \in \{1/20.4, 1/13\}$, where the scatter due to the internal motions is not large enough to cover this median trend. This is in contradiction with the idea that dynamical friction generally circularises orbits. Under the assumptions of this work, I find that the most important contributors to the stellar halo are actually affected by dynamical friction in the opposite way. Recall, however, that it is not possible to exclude that a particularly massive stellar disk in the host may affect this conclusion.
- For satellites that are massive enough, processing by dynamical friction can deprive the deposited stars of almost all memory of the initial orbital circularity of the satellite,

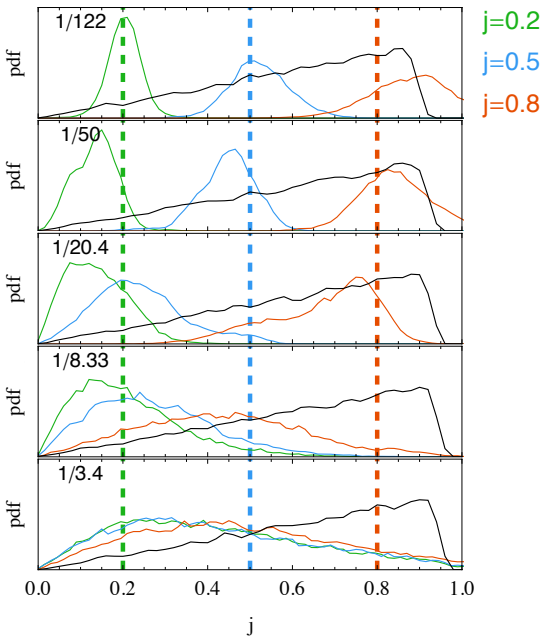

Figure 9. Final circularity distribution of the most bound 5% of the satellites particles. Dashed lines indicate the initial orbital circularity at infall. Black lines show the circularity distribution of an isotropic population ($\beta(r) = 0$).

as shown by the converging median tracks in the rightmost panel and explored quantitatively in the next Section.

5.2 Stellar circularites

Figure 9 shows the implications of these results on the deposited stellar populations: the different panels display the probability distribution of the final orbital circularities within the host for different satellite-to-host virial mass ratios. Vertical coloured lines mark the progenitors' orbital circularity at infall, for comparison. As discussed earlier, the only satellites to deposit stars on orbits that are on average more circular than the infall orbit itself (i.e. to experience orbital circularisation) are those with low-mass and with high circularity at infall. In these cases, the lack of stars with low angular momentum implies deposited stellar populations with central density holes, as it can be seen in Fig. 4. In all other cases, stars are either deposited with a mean circularity that is very similar to the orbital one at infall (in those cases in which the satellite is not massive enough or the initial orbit is already very radial), or on orbits that are more radial that the one of the progenitor at infall. In particular, for massive satellites, their significant internal velocity dispersion and processing by dynamical friction make the circularity distribution of the deposited stars almost insensitive to the orbital circularity at infall. This is clear in the cases $M_{\rm vir,s}/M_{\rm vir,h} \in \{1/8.33, 1/3.4\}$, in which the different probability distributions become similar.

Each panel of Fig. 9 also features a black profile: this shows the circularity distribution of a population that (i) lives within the same gravitational potential, (ii) has the same energy distribution as the deposited stars, (iii) has an isotropic dispersion tensor, $\beta(r) = 0$ everywhere. Here,

$$\beta(r) = 1 - \frac{\sigma_t^2(r)}{2\sigma_r^2(r)} \ , \qquad (5)$$

is the anisotropy parameter, in which σ_t and σ_r are respectively the tangential and radial velocity dispersions. Note that the isotropic populations have a significant fraction of members with high circularities. This is not the case for most stellar populations deposited by minor mergers. As a consequence, each single contribution to the stellar halo represents a radially biased kinematical population, as it will be shown in Sect. 5.4. This is not automatically true for the full halo, that is for any superposition of a set of these contributions. Populations that retain some ordered rotation, if superposed with different alignment, will result in a less marked radial bias at the expense of bulk rotation. Whether the contributions from minor mergers retain ordered rotation, by preserving a fraction of the orbital angular momentum of their progenitor, is the subject of next Section.

5.3 An atlas of kinematic profiles

Figure 10 is an atlas of stellar kinematic profiles (runs B, C, E, F). Dimensionless structural units, $\{r_{0,\rm h}, V_{\rm max,h}\}$, respectively the scale radius and maximum circular velocity of the host halo, are shown in the bottom and left axes. Top and right axes are obtained by scaling the latter dimensionless quantities for a median Milky Way like galaxy at redshift $z = 0$, $\{r_{0,\rm h}, V_{\rm max,h}\} = \{21.1{\rm kpc}, 173.1{\rm kms}^{-1}\}$. All profiles in Fig. 10 are related to concentric spherical shells. The top, middle and bottom row display respectively profiles for the radial velocity dispersion σ_r, the tangential velocity dispersion σ_t, and the ordered rotational velocity v_φ. This is the rotational velocity corresponding to the initial orbital motion of the satellite: φ is the angular direction within the orbital plane of the progenitor, $\hat{\varphi} = \hat{\mathbf{r}} \wedge \hat{\mathbf{J}}_{\rm orb}$, where $\mathbf{J}_{\rm orb}$ is the satellite's angular momentum at infall.

The clearest gradients are those displayed by the streaming velocity v_φ. At similar masses, satellites that infall on orbits with higher initial circularity deposit contributions to the stellar with a stronger rotational support, as a result of the higher initial angular momentum. Rotational support decreases strongly with satellite mass, for two reasons: (i) a higher satellite mass implies a wider scatter in the escape condition of stars, resulting in a diminished kinematical coherence; (ii) orbital angular momentum is more efficiently lost through dynamical friction.

Both streaming velocity v_φ and the two components of the velocity dispersion, σ_r and σ_t, become more and more insensitive to the satellite's orbital circularity at infall with increasing mass. This is a direct consequence of the behaviour shown by Figs. 8 and 9: processing by dynamical friction becomes more and more efficient with satellite mass, so that, together with the density profiles, the final kinematical profiles of the stars deposited by the most massive minor mergers bear hardly any memory of the initial conditions of the accretion event.

Other gradients but can be understood in terms of two basic ingredients: (i) random motions of the deposited stars around the ordered motion imprinted by the remnant's orbit increases with mass, (ii) the orbital energy within the host of stars deposited by satellites of higher masses is lower. For

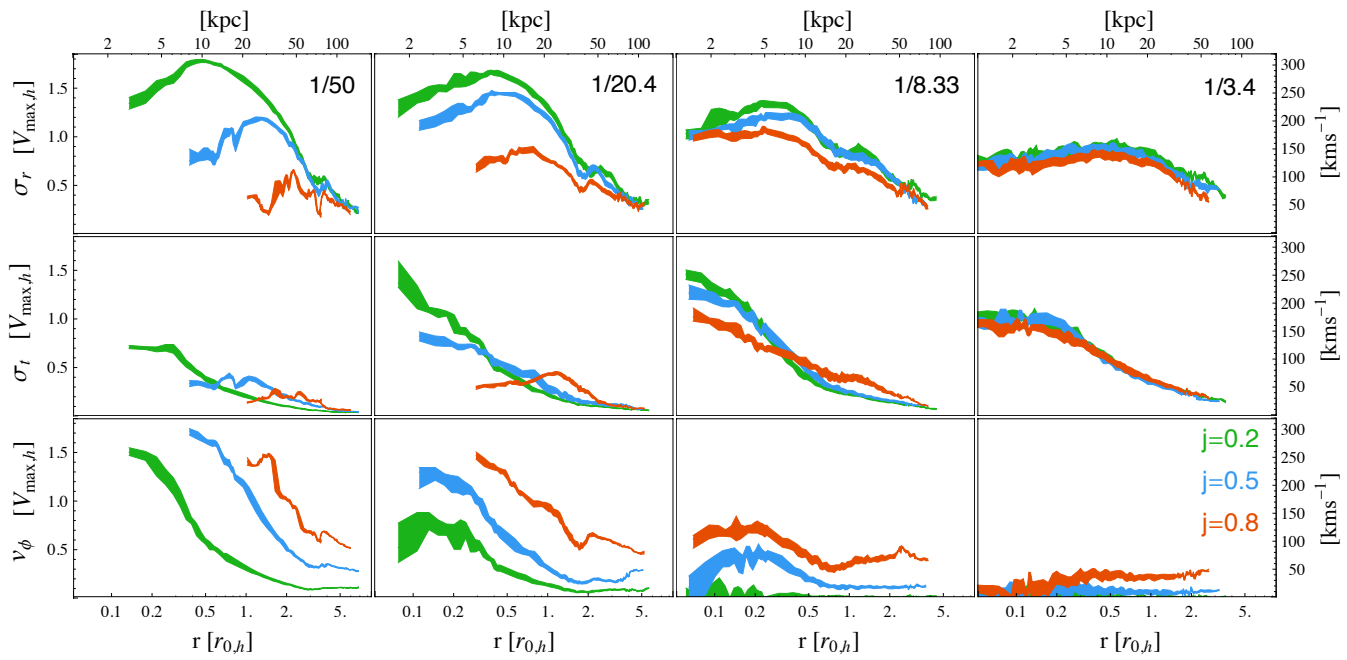

Figure 10. An atlas of the kinematical profiles of the most bound 5% of the satellites particles. The three rows of panels display respectively radial velocity dispersion σ_r, tangential velocity dispersion σ_t and ordered rotational velocity v_φ.

example, let us concentrate on the evolution with mass of the radial and tangential velocity dispersion profiles.

- A strongly radially biased population is characterised by a high radial velocity dispersion. This directly results from the mean orbital motion connected with such radial orbits, rather than from the scatter in the orbital properties of each stars around the mean. As a consequence, the radial velocity dispersion of the stellar populations contributed by the most radial accretion events decreases with satellite mass. In particular, Fig. 10 implies that, in absence of other information, stars that move at high velocity on nearly radial orbits are preferentially deposited recently by low mass satellites.
- In turn, the radial velocity dispersion of the material deposited by satellites infalling on orbits with high-circularity is mainly a result of the scatter in their specific orbital properties. Therefore, this should increase with satellite mass. However, increasing the satellite mass causes a reduction of the mean orbital energy, which reverses the trend between $M_{\rm vir,s}/M_{\rm vir,h} = 1/8.33$ and $M_{\rm vir,s}/M_{\rm vir,h} = 1/3.4$, where σ_r slightly decreases.
- A similar reasoning applies to σ_t and to its evolution with mass. Increase of random motions at the expense of ordered rotation is responsible its growth with mass while at low satellite masses. Decrease in the mean energy justifies the opposite trend at the high-mass end.

5.4 The influence of satellite concentration

Figure 11 shows how the scatter in the mass-concentration relation affects the kinematic profiles of the accreted stars. As mentioned earlier, the most concentrated satellites (or the satellites that infall on the less concentrated hosts) survive longer because of the highest density contrast, and require dynamical friction to drag them closer to the host centre before they can be efficiently stripped of their most bound particles (see Fig. 5). As a direct consequence, the average orbital energy of the deposited tagged material decreases with increasing satellite concentration, and a larger fraction of the angular momentum is lost.

This is clearly seen in the profiles displayed in Fig. 11. (i) The ordered rotation v_φ retained within the stellar populations decreases monotonically with the satellite concentration. (ii) Radial and tangential velocity dispersion profiles are clearly ordered with concentration. Both these points are especially true for the material deposited closer and closer to the host's centre, which has experienced an increasing amount of dynamical friction and has more and more bound energy values within the host.

Despite the gradual loss of ordered motion with growing satellite concentration, the radial bias in the different cases remains very similar (bottom-right panel). While the evolution of both σ_r and σ_t is significant, this takes place in a coherent manner, so that their ratio is largely insensitive to concentration, and each single contribution remains largely radially biased. As already mentioned earlier, it should be kept in mind that a superposition of populations rotating in different directions may be less radial than the single components. This effect, though, will not be significant when the major contributions come from satellites that have had their orbital angular momentum largely consumed by dynamical friction.

6 DISCUSSION AND CONCLUSIONS

Without aiming to produce realistic examples of galactic stellar haloes, here I have investigated the influence of the different physical ingredients that shape the contributions

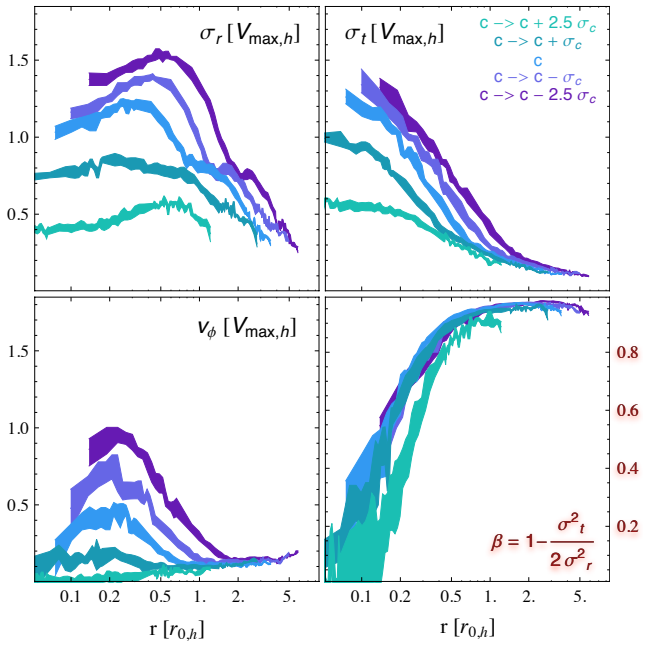

Figure 11. The effect of the satellite's concentration on the kinematics of the deposited material, assuming f_{mb} selects the most bound 5%. Displayed profiles pertain to runs E and H, with $M_{\mathrm{vir,s}}/M_{\mathrm{vir,h}} = 1/8.33$ and $j_{\mathrm{inf}} = 0.5$.

of each single accretion event. This exercise is a useful first step towards the interpretation of results of both recent numerical investigations into the detailed properties of stellar haloes (e.g, Abadi et al. 2006; Cooper et al. 2010, 2013; Tissera et al. 2014; Pillepich et al. 2014; Rodriguez-Gomez et al. 2015); and observational campaigns targeting the outer faint envelopes of our own and nearby galaxies (e.g., Jurić et al. 2008; Sesar et al. 2011; Deason et al. 2011, 2014; Gilbert et al. 2012; Ibata et al. 2014; van Dokkum et al. 2014; Duc et al. 2015; Monachesi et al. 2015b; Trujillo & Fliri 2015).

6.1 Limits of this study

There are several limitations to the present study.

• Some derive from the simplifying assumptions of ideal, spherical hosts and satellites. The most evident in this category is the lack of a disk component in the gravitational potential of the host, which is known to have a role in the general process of tidal disruption. First, it accelerates the disruption of subhaloes through disk shocking (e.g., D'Onghia et al. 2010a), and second, it contributes an additional torque that tends to align satellites with the disk plane (e.g., Peñarrubia et al. 2004). Ignoring these two effects, however, does not invalidate the analyses of this work for the following reasons. First, the contribution of tidal shocking is only crucial to the evolution of subhaloes with low virial mass, in a regime that is not relevant here ($M_{\mathrm{vir,s}} \lesssim 10^9 M_\odot$, D'Onghia et al. 2010a), and is of little importance for those subhaloes that actually contribute the largest amount of ex-situ material to the stellar halo of Milky Way like galaxies. Second, I have not addressed 'local' properties of the accreted halo, or tried to explore the differences of properties along particular directions. The presence of the host disk may induce differences in the accreted halo along directions oriented differently with respect to it (e.g., Monachesi et al. 2015a), and it is clear that this paper cannot address this. In fact, I have concentrated on averages obtained in spherical shells, which the presence or absence of a stellar disk leaves largely unaffected.

• Other limitations follow more directly from the use of a particle tagging technique. These are shared with those studies that have addressed the build up of the accreted stellar halo within a similar framework (e.g., Bullock & Johnston 2005; Cooper et al. 2010). The major implicit assumptions that lie within the tagging technique itself are that (i) the gravitational influence of the stellar component of the satellite and (ii) the detailed morphological properties of the satellite can both be ignored. However, it is known that structural properties can significantly affect the the post-infall evolution of the satellite (e.g., D'Onghia et al. 2010b; Kazantzidis et al. 2011; Chang et al. 2013), and it is therefore worth checking in which regime a particle tagging technique can be safely adopted.

The assumption (i) is clearly broken in the case of a satellite featuring a baryon-dominated, concentrated central component, like a central bulge. Density in such region would be significantly higher than in embedding NFW halo, and therefore such component would be more resilient to tidal stripping. Prolonged dynamical friction might affect the deposition of the stellar material, possibly introducing differences from what predicted by a particle tagging implementation. For example, it follows that particle tagging is not directly viable to study the accreted stellar haloes of massive galaxies. These receive substantial contributions by satellites with virial masses comparable to the one of the Milky Way, characterised by baryon-dominated centers which are more dense than their NFW haloes. In turn, the stellar halo of a Milky Way like galaxy is contributed by satellites with $M_{\mathrm{vir,s}} \lesssim 10^{11} M_\odot$, which have been shown to be dark matter dominated at all radii (e.g., Walker et al. 2009; Amorisco & Evans 2011; Collins et al. 2014; Veljanoski et al. 2015).

The assumption (ii) is broken when the actual orbital structure of the satellite stars is significantly different from the approximately isotropic, pressure supported central regions of an NFW halo. This is the case when the satellite features a rotationally supported thin-disk satellite, which is known to respond to tides differently from a spheroid (e.g., D'Onghia et al. 2010a; Chang et al. 2013; Peñarrubia et al. 2010). In such a case, the predictions of a particle tagging technique would not be reliable. For example, D'Onghia et al. (2010b) points out the differences in the post infall evolution of a disky satellite that spins with a prograde/retrograde alignment and Chang et al. (2013) shows that the removal of the satellite's stellar component is substantially more efficient when the morphology is the one of a thin stellar disk rather than a spheroid. However, the dwarf members of the Local Group display very limited rotational support, with quite low values of the dimensionless parameter v/σ (e.g., Mayer et al. 2001; McConnachie 2012; Wheeler et al. 2015). Even in those cases in which a velocity gradient is detected, their morphology remains far from the one of thin disks, and is substantially puffy (see e.g., van der Marel & Cioni 2001; Leaman et al. 2012). Cooper et al. (2010) has shown explicitly that both density and kinemat-

ics of the dwarf Spheroidal satellites of the Milky Way are well described by the most bound particles of an NFW halo.

While the arguments above support the robustness of the results of this work, the present objective remains to identify and explain the main correlations and physical mechanisms, rather than to provide precise predictions for any individual halo. Here I have concentrated mainly on the global properties related to the process of mass deposition, like the mean energy or the half-mass radius, and on the kinematics of the different contributions.

6.2 Summary

Each individual contribution to the accreted stellar halo is defined within a parameter space of high dimensionality. For Milky Way like masses and below only a handful of major contributions shape the resulting accreted halo, a number that is not high enough to allow for the properties of such haloes to converge. In this regime, therefore, the halo formation process remains highly stochastic, resulting in significant halo-to-halo scatter. Here, I have adopted a simplified approach to explore and classify the main degrees of freedom of the problem, and to deconstruct their influence in shaping stellar deposition by individual satellites. Namely, I have concentrated on the mass ratio of each accretion event, the internal structure of the satellite itself (in the form of its concentration and of the 'size' of its stellar component, $f_{\rm mb}$), the infall redshift and the properties of the orbit at infall (its energy and circularity).

Main results are summarised below.

- Massive satellites sink deeper into the gravitational potential of the host before stars are lost, so that these are contributed at smaller radii within the host. In turn, low-mass satellites survive much longer, but dynamical friction is not capable of dragging them within the innermost regions, with a clear segregation (see also Rodriguez-Gomez et al. 2015, who find clear evidence for this segregation in the accreted stellar haloes of the Illustris galaxies). Depending on their initial orbital circularity at infall and their concentration, satellites with $M_{\rm vir,s}/M_{\rm vir,h} \lesssim 1/50$ may still display bound remnants at the end of the simulations (equivalent to 15 Gyr for a host with $M_{\rm vir,h} = 10^{12} M_{\odot}$).
- Satellites that are accreted at higher redshift deposit their material at smaller radii within the host, as a result of the fact that the host was physically smaller at that time and that the orbital energy at accretion was lower.
- The mass-concentration relation has a scatter that is wide enough to invert the ordering with mass: satellites that are one-sigma more (less) concentrated than average can deposit their stars at radii that are closer in (further out), as a factor of ≈ 2.5 in mass (and average concentration) would imply. In turn, the scatter in the distribution of orbital energies at infall is not as important.
- Dynamical friction can imply a marked evolution in the orbital properties of the remnant, shaping both density distribution and kinematics of the deposited material.
- Low-mass satellites infalling on high-circularity orbits experience some mild circularisation, and result in density profiles that feature central density holes. The dominating effect of dynamical friction on satellites with $M_{\rm vir,s}/M_{\rm vir,h} \gtrsim 1/20$ is to quickly radialise their orbits, up to erasing memory of the initial infall circularity.
- Material deposited by low mass satellites retains a significant amount of ordered rotation and, because of the extended orbits, also features high radial velocity dispersion. In turn, angular momentum is consumed and diluted in the more massive accretion events, resulting in almost non rotating contributions, with a strong radial bias.

Finally, minor mergers have been suggested as a driver of the size evolution of massive elliptical galaxies with redshift (e.g. Bezanson et al. 2009; Naab et al. 2009; Feldmann et al. 2010; van Dokkum et al. 2010; Oser et al. 2010, 2012, and references therein). Indeed, here I am showing that mergers with increasingly low virial mass ratios result in stellar deposition increasingly large radii around the host. This is a result of the switching balance between the rate at which satellites are stripped by tides and the rate at which they sink trough dynamical friction. For hosts and satellites that populate the regions of parameter space that is interesting for a ΛCDM universe, dynamical friction is faster than stripping for the massive minor mergers, resulting in stellar deposition within the inner regions of the host. On the other hand, and despite the slow rate of tidal stripping, dynamical friction is too slow to drag the low mass satellites towards the centre of the host. Similarly, orbital evolution of the remnant is only effective at the high-mass end, where it can operate significantly before stars are lost. In these cases, it radialises the orbit of the progenitor satellite, with consequences on the kinematics of the deposited population, but also with possibly interesting effects in shaping the morphologies of low surface brightness tidal features (Amorisco 2015; Hendel & Johnston 2015).

ACKNOWLEDGMENTS

It is a pleasure to thank Annalisa Pillepich and Glenn van de Ven for stimulating conversations, Simon White for insightful comments and the anonimous referee for a constructive report. The Dark Cosmology Centre is funded by the DNRF.

REFERENCES

Abadi, M. G., Navarro, J. F., & Steinmetz, M. 2006, MNRAS, 365, 747
Amorisco, N. C., & Evans, N. W. 2011, MNRAS, 411, 2118
Amorisco, N. C. 2015, MNRAS, 450, 575
Atkinson, A. M., Abraham, R. G., & Ferguson, A. M. N. 2013, ApJ, 765, 28
Barnes, J. E. 1988, ApJ, 331, 699
Belokurov, V., Zucker, D. B., Evans, N. W., et al. 2006, ApJL, 642, L137
Benson, A. J. 2005, MNRAS, 358, 551
Bezanson, R., van Dokkum, P. G., Tal, T., et al. 2009, ApJ, 697, 1290
Boylan-Kolchin, M., Ma, C.-P., & Quataert, E. 2008, MNRAS, 383, 93
Buist, H. J. T., & Helmi, A. 2014, AA, 563, A110
Bullock, J. S., Kravtsov, A. V., & Weinberg, D. H. 2001, ApJ, 548, 33
Bullock, J. S., & Johnston, K. V. 2005, ApJ, 635, 931

Chandrasekhar, S. 1943, ApJ, 97, 255
Chang, J., Macciò, A. V., & Kang, X. 2013, MNRAS, 431, 3533
Cohen, J. G., Sesar, B., Banholzer, S., & PTF Consortium, t. 2015, arXiv:1509.05997
Collins, M. L. M., Chapman, S. C., Rich, R. M., et al. 2014, ApJ, 783, 7
Cooper, A. P., Cole, S., Frenk, C. S., et al. 2010, MNRAS, 406, 744
Cooper, A. P., D'Souza, R., Kauffmann, G., et al. 2013, MNRAS, 434, 3348
Crnojević, D., Sand, D. J., Spekkens, K., et al. 2016, ApJ, 823, 19
Deason, A. J., Belokurov, V., & Evans, N. W. 2011, MNRAS, 416, 2903
Deason, A. J., Belokurov, V., Evans, N. W., & Johnston, K. V. 2013, ApJ, 763, 113
Deason, A. J., Belokurov, V., Koposov, S. E., & Rockosi, C. M. 2014, ApJ, 787, 30
Diemand, J., Moore, B., & Stadel, J. 2004, MNRAS, 352, 535
D'Onghia, E., Springel, V., Hernquist, L., & Keres, D. 2010, ApJ, 709, 1138
D'Onghia, E., Vogelsberger, M., Faucher-Giguere, C.-A., & Hernquist, L. 2010, ApJ, 725, 353
D'Souza, R., Kauffman, G., Wang, J., & Vegetti, S. 2014, MNRAS, 443, 1433
Duc, P.-A., Cuillandre, J.-C., Karabal, E., et al. 2015, MNRAS, 446, 120
Eddington, A. S. 1916, MNRAS, 76, 572
Eggen, O. J., Lynden-Bell, D., & Sandage, A. R. 1962, ApJ, 136, 748
Errani, R., Peñarrubia, J., & Tormen, G. 2015, MNRAS, 449, L46
Fakhouri, O., Ma, C.-P., & Boylan-Kolchin, M. 2010, MNRAS, 406, 2267
Feldmann, R., Carollo, C. M., Mayer, L., et al. 2010, ApJ, 709, 218
Fellhauer, M., & Lin, D. N. C. 2007, MNRAS, 375, 604
Fujii, M., Funato, Y., & Makino, J. 2006, PASJ, 58, 743
Gao, L., White, S. D. M., Jenkins, A., Stoehr, F., & Springel, V. 2004, MNRAS, 355, 819
Gao, L., Navarro, J. F., Cole, S., et al. 2008, MNRAS, 387, 536
Gilbert, K. M., Guhathakurta, P., Beaton, R. L., et al. 2012, ApJ, 760, 76
Grillmair, C. J. 2009, ApJ, 693, 1118
Hashimoto, Y., Funato, Y., & Makino, J. 2003, ApJ, 582, 196
Hendel, D., & Johnston, K. V. 2015, MNRAS, 454, 2472
Hopkins, P. F., Lauer, T. R., Cox, T. J., Hernquist, L., & Kormendy, J. 2009, ApJS, 181, 486
Ibata, R. A., Gilmore, G., & Irwin, M. J. 1995, MNRAS, 277, 781
Ibata, R., Martin, N. F., Irwin, M., et al. 2007, ApJ, 671, 1591
Ibata, R. A., Lewis, G. F., McConnachie, A. W., et al. 2014, ApJ, 780, 128
Jiang, I.-G., & Binney, J. 2000, MNRAS, 314, 468
Jiang, L., Cole, S., Sawala, T., & Frenk, C. S. 2015, MNRAS, 448, 1674
Johnston, K. V. 1998, ApJ, 495, 297
Johnston, K. V., Bullock, J. S., Sharma, S., et al. 2008, ApJ, 689, 936
Jurić, M., Ivezić, Ž., Brooks, A., et al. 2008, ApJ, 673, 864
Kazantzidis, S., Magorrian, J., & Moore, B. 2004, ApJ, 601, 37
Kazantzidis, S., Łokas, E. L., Callegari, S., Mayer, L., & Moustakas, L. A. 2011, ApJ, 726, 98
Kravtsov, A. V., Gnedin, O. Y., & Klypin, A. A. 2004, ApJ, 609, 482
Kuhlen, M., Diemand, J., & Madau, P. 2007, ApJ, 671, 1135
Leaman, R., Venn, K. A., Brooks, A. M., et al. 2012, ApJ, 750, 33
Ludlow, A. D., Navarro, J. F., Springel, V., et al. 2009, ApJ, 692, 931
Ludlow, A. D., Navarro, J. F., Angulo, R. E., et al. 2014, MNRAS, 441, 378
Martínez-Delgado, D., Peñarrubia, J., Gabany, R. J., et al. 2008, ApJ, 689, 184
Martínez-Delgado, D., Gabany, R. J., Crawford, K., et al. 2010, AJ, 140, 962
Mayer, L., Governato, F., Colpi, M., et al. 2001, ApJL, 547, L123
Mayer, L., Governato, F., Colpi, M., et al. 2001, ApJ, 559, 754
McConnachie, A. W., Irwin, M. J., Ibata, R. A., et al. 2009, Nat, 461, 66
McConnachie, A. W. 2012, AJ, 144, 4
Monachesi, A., Bell, E. F., Radburn-Smith, D., et al. 2015, arXiv:1507.06657
Monachesi, A., Gomez, F. A., Grand, R. J. J., et al. 2015, arXiv:1512.03064
Muñoz-Cuartas, J. C., Macciò, A. V., Gottlöber, S., & Dutton, A. A. 2011, MNRAS, 411, 584
Naab, T., Johansson, P. H., & Ostriker, J. P. 2009, ApJL, 699, L178
Navarro, J. F., Frenk, C. S., & White, S. D. M. 1997, ApJ, 490, 493
Oser, L., Ostriker, J. P., Naab, T., Johansson, P. H., & Burkert, A. 2010, ApJ, 725, 2312
Oser, L., Naab, T., Ostriker, J. P., & Johansson, P. H. 2012, ApJ, 744, 63
Peñarrubia, J., Just, A., & Kroupa, P. 2004, MNRAS, 349, 747
Peñarrubia, J., Navarro, J. F., & McConnachie, A. W. 2008, ApJ, 673, 226-240
Peñarrubia, J., Belokurov, V., Evans, N. W., et al. 2010, MNRAS, 408, L26
Pillepich, A., Vogelsberger, M., Deason, A., et al. 2014, MNRAS, 444, 237
Rodriguez-Gomez, V., Pillepich, A., Sales, L. V., et al. 2015, arXiv:1511.08804
Sales, L. V., Navarro, J. F., Abadi, M. G., & Steinmetz, M. 2007, MNRAS, 379, 1464
Searle, L., & Zinn, R. 1978, ApJ, 225, 357
Sesar, B., Jurić, M., & Ivezić, Ž. 2011, ApJ, 731, 4
Springel, V. 2005, MNRAS, 364, 1105
Springel, V., Wang, J., Vogelsberger, M., et al. 2008, MNRAS, 391, 1685
Taylor, J. E., & Babul, A. 2001, ApJ, 559, 716
Tissera, P. B., Beers, T. C., Carollo, D., & Scannapieco, C. 2014, MNRAS, 439, 3128

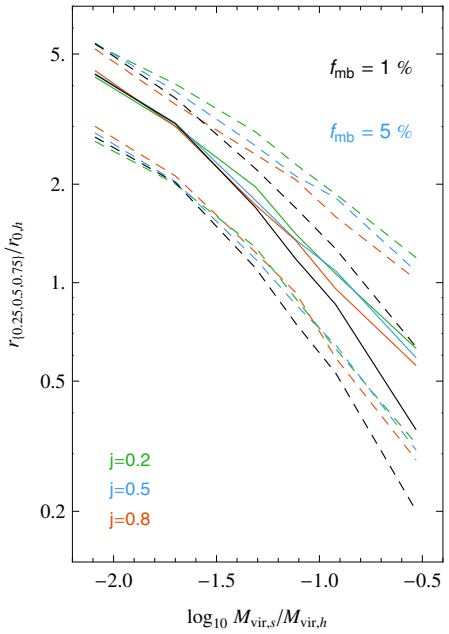

Figure A1. The 25%-, 50%- and 75%- mass radii for the density profiles generated assuming $f_{\rm mb} = 5\%$ (profiles coloured according to circularity at infall, like in Fig. 3 and 4) and $f_{\rm mb} = 1\%$ (black profiles, $j = 0.5$).

Tomozeiu, M., Mayer, L., & Quinn, T. 2016, ApJ, 818, 193
Trujillo, I., & Fliri, J. 2015, arXiv:1510.04696
van den Bosch, F. C., Jiang, F., Campbell, D., & Behroozi, P. 2015, arXiv:1510.01586
van der Marel, R. P., & Cioni, M.-R. L. 2001, AJ, 122, 1807
van Dokkum, P. G., Abraham, R., & Merritt, A. 2014, ApJL, 782, L24
van Dokkum, P. G., Whitaker, K. E., Brammer, G., et al. 2010, ApJ, 709, 1018
Velazquez, H., & White, S. D. M. 1999, MNRAS, 304, 254
Veljanoski, J., Mackey, A. D., Ferguson, A. M. N., et al. 2014, MNRAS, 442, 2929
Veljanoski, J., Ferguson, A. M. N., Mackey, A. D., et al. 2015, MNRAS, 452, 320
Vogelsberger, M., Genel, S., Springel, V., et al. 2014, MNRAS, 444, 1518
Walker, M. G., Mateo, M., Olszewski, E. W., et al. 2009, ApJ, 704, 1274
Wetzel, A. R. 2011, MNRAS, 412, 49
Wheeler, C., Pace, A. B., Bullock, J. S., et al. 2015, arXiv:1511.01095
White, S. D. M. 1978, MNRAS, 184, 185
White, S. D. M. 1980, MNRAS, 191, 1P
White, S. D. M., & Frenk, C. S. 1991, ApJ, 379, 52
Widrow, L. M. 2000, ApJS, 131, 39

APPENDIX A: TAGGING FRACTION AND HALF-MASS RADII

Fig. A1 displays the dependence on the virial mass ratio of the minor merger, $M_{\rm vir,s}/M_{\rm vir,h}$, of the radii containing $\{25\%, 50\%, 75\%\}$ of the contributed stellar mass, respectively $\{r_{0.25}, r_{0.5}, r_{0.75}\}$. Additionally, Fig. A1 shows the effect of lowering the tagging fraction, from the nominal value used throughout the paper, $f_{\rm mb} = 5\%$, to $f_{\rm mb} = 1\%$ (black profiles, for an initial circularity of $j = 0.5$). For the satellites with the lowest mass, this does not introduce any noticeable difference. This follows from the fact that dynamical friction is not capable of consuming any more energy within the interval of time that separates the loss of the 5% particles and the escape of the 1% particles. However, more massive satellites do experience additional dynamical friction within this interval of time, and therefore density profiles generated using $f_{\rm mb} = 1\%$ have smaller characteristic radii.